#### **PAPER**

## Bremsstrahlung hard x-ray source driven by an electron beam from a self-modulated laser wakefield accelerator

To cite this article: N Lemos et al 2018 Plasma Phys. Control. Fusion 60 054008

View the article online for updates and enhancements.

#### Related content

- Self-modulated laser wakefield accelerators as x-ray sources
  N Lemos, J L Martins, F S Tsung et al.
- Applications of laser wakefield acceleratorbased light sources
  Félicie Albert and Alec G R Thomas
- Measuring the angular dependence of betatron x-ray spectra in a laser-wakefield accelerator

F Albert, B B Pollock, J L Shaw et al.

#### Recent citations

- All-optical generation of petawatt gamma radiation via inverse Compton scattering from laser interaction with tube target
  T Y Long et al
- Effects of laser polarization and wavelength on hybrid laser wakefield and direct acceleration Xi Zhang et al



### IOP ebooks™

Bringing you innovative digital publishing with leading voices to create your essential collection of books in STEM research.

Start exploring the collection - download the first chapter of every title for free.

# Bremsstrahlung hard x-ray source driven by an electron beam from a self-modulated laser wakefield accelerator

N Lemos<sup>1,6</sup>, F Albert<sup>1</sup>, J L Shaw<sup>2</sup>, D Papp<sup>3</sup>, R Polanek<sup>3</sup>, P King<sup>1,4</sup>, A L Milder<sup>2</sup>, K A Marsh<sup>5</sup>, A Pak<sup>1</sup>, B B Pollock<sup>1</sup>, B M Hegelich<sup>4</sup>, J D Moody<sup>1</sup>, J Park<sup>1</sup>, R Tommasini<sup>1</sup>, G J Williams<sup>1</sup>, Hui Chen<sup>1</sup> and C Joshi<sup>5</sup>

E-mail: candeiaslemo1@llnl.gov

Received 8 December 2017, revised 21 February 2018 Accepted for publication 2 March 2018 Published 22 March 2018



#### **Abstract**

An x-ray source generated by an electron beam produced using a Self-Modulated Laser Wakefield Accelerator (SM-LWFA) is explored for use in high energy density science facilities. By colliding the electron beam, with a maximum energy of 380 MeV, total charge of >10 nC and a divergence of  $64\times100$  mrad, from a SM-LWFA driven by a 1 ps 120 J laser, into a high-Z foil, an x/gamma-ray source was generated. A broadband bremsstrahlung energy spectrum with temperatures ranging from 0.8 to 2 MeV was measured with an almost 2 orders of magnitude flux increase when compared with other schemes using LWFA. GEANT4 simulations were done to calculate the source size and divergence.

Keywords: bremsstrahlung, x-ray source, gamma-ray source, self-modulated laser wakefield accelerator

1

(Some figures may appear in colour only in the online journal)

#### 1. Introduction

Matter can be driven to extreme states of temperature and pressure in many subfields of physics such as astrophysics, High Energy Density Science (HEDS) and inertial confinement fusion (ICF). With the remarkable advances in material and laser science, HEDS facilities can now start to access these exotic physical conditions (albeit for a short duration) using high-power lasers. HED plasmas are in a non-equilibrium, transient state and can be extremely difficult to diagnose. To diagnose such transient and extreme states of matter, a very hard x-ray/gamma-ray source with a high-photon yield (>10<sup>10</sup>

photons), short pulse duration (fs-ps), broad-energy spectrum (keV to MeV) and source sizes ranging from microns to tens of microns is desirable. Within this context, bremsstrahlung-based sources can be very attractive. They are being used for flash radiography [1], to radiograph double-shell ignition targets [2], to probe ICF implosion targets using Compton radiography [3], and to produce high-resolution imaging in non-destructive testing [4]. Many of the high power lasers used for HEDS possess picosecond lasers that can be used to generate secondary sources, including bremsstrahlung.

Bremsstrahlung radiation is generated when an electron passes in the vicinity of the nucleus of an atom. The Coulomb force of the nucleus deflects the electrons, and due to energy conservation, the lost 'braking' energy is emitted as a high-energy

<sup>&</sup>lt;sup>1</sup> Lawrence Livermore National Laboratory, NIF and Photon Sciences, 7000 East Avenue, Livermore, CA 94550, United States of America

<sup>&</sup>lt;sup>2</sup> Laboratory for Laser Energetics, University of Rochester, 250 E River Rd, Rochester, NY 14623 United States of America

<sup>&</sup>lt;sup>3</sup> ELI-ALPS, ELI-HU Non-profit Ltd, Szeged, Hungary

<sup>&</sup>lt;sup>4</sup> Department of Physics, University of Texas at Austin, Austin, TX 78712, United States of America

<sup>&</sup>lt;sup>5</sup> Department of Electrical Engineering, University of California Los Angeles, 405 Hilgard Ave, Los Angeles, CA 90095, United States of America

<sup>&</sup>lt;sup>6</sup> Author to whom any correspondence should be addressed.

photon. If the electron comes to a total stop, all its energy is converted into the photon energy. Therefore, the maximum energy of the hard x-ray beam will match the maximum electron energy. A high-Z material is used because the higher-charge nucleus increases the bremsstrahlung conversion efficiency. Thicker materials (up to a limit where radiation would be reabsorbed) are also ideal to maximize the number of interactions between the electrons and the nuclei. Bremsstrahlung sources are usually generated in HEDS facilities by focusing a laser directly onto a high-Z solid material, which produces a hot electron population that in turn generates high-energy photons through bremsstrahlung [5–10]. If the laser pulse is relativistic  $(a_0 > 1)$ , the plasma electrons are heated to very high temperature by a variety of mechanisms. Here  $a_0 = eA/mc^2$  is the normalized vector potential of the laser pulse, where e is the electron charge, A the laser vector potential, m the electron mass and c is the speed of light. For instance, electrons can be accelerated by the ponderomotive  $j \times B$  acceleration process in the forward direction over a large range of angles and subsequently generate bremsstrahlung radiation that has a much larger source size (>200  $\mu$ m) and is almost isotropic  $(4\pi)$  [11].

A recently proposed alternative to these bremsstrahlung sources is to focus a high-intensity laser in a gas jet to produce an electron beam through laser wakefield acceleration (LWFA) [12] and then collide the electron beam with a high-Z solid target [4, 13–16]. This scheme has two main advantages: first, the electron beam has a very low divergence, which reduces the divergence of the subsequent bremsstrahlung emission; the electron beam can reach much higher energies thereby generating higher energy bremsstrahlung photons. It has been shown that such a gas jet electron source-solid target x-ray converter configuration is more efficient at producing bremsstrahlung emission [11, 13] than directly focusing the laser on the solid material. For instance, [13] shows an increase of  $\sim$ 6 times of the peak radiation dose produced when using a gas jet. In a LWFA the laser can transfer its energy into plasma waves that in turn accelerate the electrons to relativistic energies with a reasonable yield with a very small source size and divergence angle making this process very attractive for bremsstrahlung generation. As a result, the generated hard x-ray source has a high yield, a source size on the order of the electron beam size (few microns) and an angular spread of a few degrees. The gas jet-solid target configuration has been shown to produce directional electrons and therefore hard x-ray beams when the LWFA is operated in the blowout regime [4, 15–21]. Although these sources have extremely good time (fs) and spatial (tens of microns) resolution (tens of microns), the photon yield is still low for HEDS due to the relatively low charge electron beams (hundreds of pCs).

In this work, we adapt LWFA-based bremsstrahlung sources to lasers available at HEDS facilities. We propose to increase the charge of the electron beam by at least one order of magnitude by using a Self-Modulated LWFA (SM-LWFA) [22–24]. We show that by using a typical ps laser present at a HEDS facility it is possible to access the SM-LWFA regime and produce a high-energy, high-charge (several nC), low-divergence electron beam that can be collided with a high-Z foil to increase the yield of the hard x-rays that are generated.

This paper is organized as follows. In section 2, a brief background of SM-LWFA is given. In section 3 the experimental setup is described. The experimental results for the electron and hard x-ray beams are presented and discussed in sections 4 and 5, respectively. Section 6 states the conclusions.

#### 2. Background—SM-LWFA as an electron source

To drive a SM-LWFA, a high-intensity laser pulse with a pulse duration (1 ps, 300  $\mu$ m) larger than the plasma period ( $\sim$ 10  $\mu$ m for a 10<sup>19</sup> cm<sup>-3</sup> plasma density) is propagated through an underdense plasma. It can generate plasma waves through the Raman Forward Scattering (RFS) and SM instabilities of the laser pulse [24]. Therefore, the index of refraction in the plasma is no longer constant and will oscillate periodically at the plasma wavelength, which modulates the laser pulse envelope through the creation of Stokes and anti-Stokes sidebands to the pump frequency. This modulated laser beam will in turn resonantly amplify the plasma wave, which can reach electrical fields of several GeV cm<sup>-1</sup>. These plasma waves have an associated longitudinal and transverse field. The background plasma electrons are heated by the process known as stochastic heating [25], and some of these electrons become energetic enough to be trapped by the plasma wave and accelerated to several hundred MeV. The transverse field leads to betatron-like oscillations of the off-axis electrons, which causes them to radiate photons in the forward direction and generate an x-ray beam [26]. Furthermore, since the laser pulse will naturally overlap many plasma wavelengths and therefore the accelerating electrons, there is a significant contribution from direct laser acceleration (DLA) [27-30] to the energy gained by the electrons [31]. In this work, the pulse duration was on the order of 1 ps (300  $\mu$ m) and the plasma period was  $\sim 10 \,\mu \text{m}$ , thus the laser overlaps  $\sim 30 \text{ plasma periods}$ .

#### 3. Experimental setup

This experiment was performed at the Jupiter Laser Facility at Lawrence Livermore National Laboratory. The laser beam was produced by a Nd:glass chirped pulse amplification laser system with an energy of 120 J (on target), average pulse duration of  $0.7^{+0.3}_{-0.1}$  ps (FWHM), central wavelength of 1053 nm, repetition rate of 30 min and an initial beam diameter of 22 cm. Figure 1 shows a schematic of the experimental setup and the diagnostics used in the experiment. The main beam was focused with an f/10 off-axis parabola 100  $\mu$ m inside a 4 mm wide column of Helium gas created by a supersonic nozzle [32]. The vacuum spot size  $w_0$  was 29  $\mu$ m  $(1/e^2)$  intensity point) measured with the laser operating at low power. The peak intensity was  $1.1 \times 10^{19} \,\mathrm{W \, cm^{-2}}$  giving an  $a_0$  of 3. A probe beam, with a central wavelength of 527 nm and a pulse duration of 1 ps (FWHM), was used to probe the plasma transversely. After crossing the plasma, the probe beam entered a folded interferometer that generated both interferometry, to measure the plasma electron density profile,

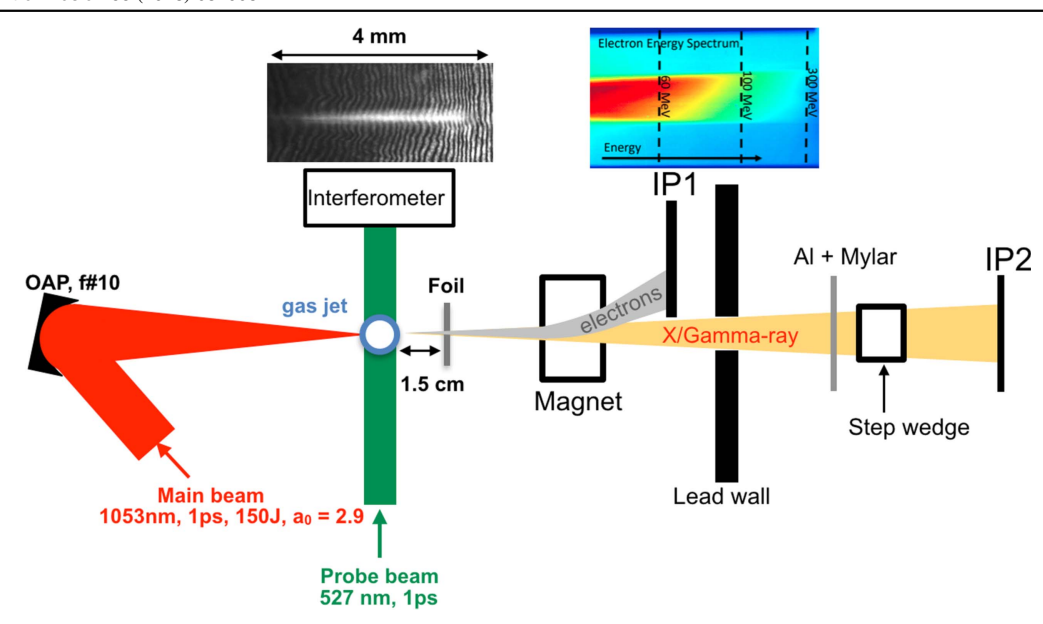


**Figure 1.** Experimental setup for generating Bremsstrahlung radiation from relativistic electrons produced by SM-LWFA at the Jupiter Laser Facility using the Titan Laser. The Titan laser (red beam) is focused by an OAP into a 4 mm supersonic gas jet. The probe beam (green) crosses the plasma generated by the main beam and goes into a folded interferometer. An example of an interferogram is shown next to the interferometer. The bright region in the center of the interferogram is due to the radiation produced by the rapidly accelerating electrons [33]. The electrons (gray line) collide with a foil (Ta or W) to generate the hard x-ray beam and are dispersed by the 1 T magnet centered on the laser axis (12 cm from the source inside the target chamber) and recorded by an image plate. An example of the electron spectrum recorded at image plate 1 (IP1) is shown. A lead wall with an opening of  $10 \times 5$  cm is placed 80 cm after the gas jet to block the background noise generated inside the chamber. At the exit of the vacuum chamber, the hard x-rays go through an Aluminum and Mylar filter. After exiting the vacuum chamber, the photons (brown line) propagate through 36 step wedge filters onto image plate 2 (IP2).

and shadowgraphy, to give the plasma shape and length. This beam is timed to arrive just after the main beam exits the gas jet. The typical plasma electron density profile consists of a 500  $\mu$ m density up-ramp followed by a 3000  $\mu$ m plateau with a density  $n_e = 5 \times 10^{18} \, \mathrm{cm}^{-3}$  and then a 500  $\mu$ m density down ramp. The electrons (gray beam) are accelerated in the gas jet and collide with a metal foil placed 1.5 cm after the nozzle to generate the hard x-rays through bremsstrahlung. Two foil materials were used: tungsten (W) with thicknesses of 0.5 or 1 mm and tantalum (Ta) with a 1 mm thickness.

The electron beam was then dispersed onto an image plate (IP1) by a 1 Tesla dipole magnet. The hard x-rays generated in the foil pass through an opening in a lead wall that blocks the background noise generated inside the vacuum chamber and exit the chamber through an aluminum and mylar filter. Outside the chamber, these high-energy photons pass through a step wedge filter [3, 34–37], which consists of an array of 36 different filters of Ta and Al with variable thickness, and are recorded by IP2. The weakest filter starts transmitting radiation above 20 keV and the strongest at 300 keV (figure 2). The final signal seen on IP2 must be corrected for the transmission function of the step wedge, the transmission function of the Al and Mylar window at the exit of the chamber, and by the sensitivity and efficiency of the IP2 [38] (figure 2). The angle covered by the step-wedge diagnostic was ~0.5°, smaller than the expected divergence of a few degrees for the bremsstrahlung radiation and that of the divergence of  $\sim 3^{\circ}$  of the electron beam.

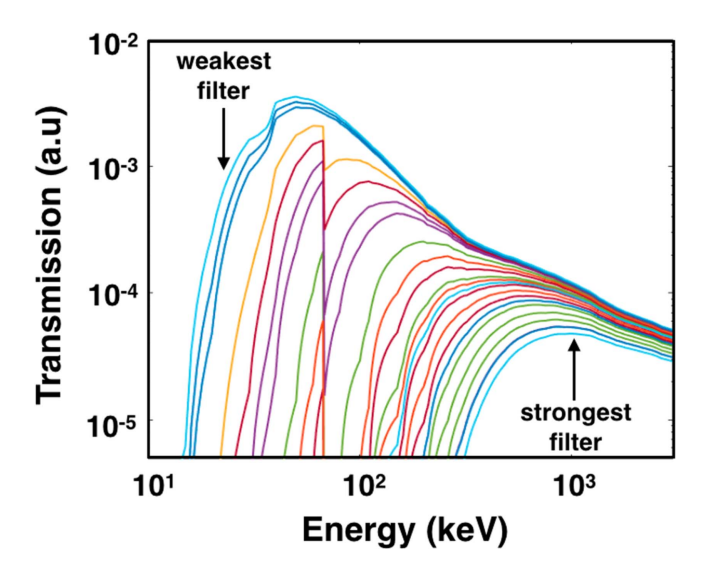


**Figure 2.** Response function of each of the 36 individual filters for different photon energies taking into account the transmission function of the Al and Mylar window at the exit of the chamber and the sensitivity and efficiency of the IP2. The curves are organized from the weakest (top) to the strongest filter (bottom).

#### 4. Electron beam characterization

In this work, we first characterize the electron beam energy spectrum, divergence, shape and charge. In order to avoid any distortions to the electron beam caused by the foil, the characterization was done without the foil after the nozzle. An example of the electron energy spectrum is shown in

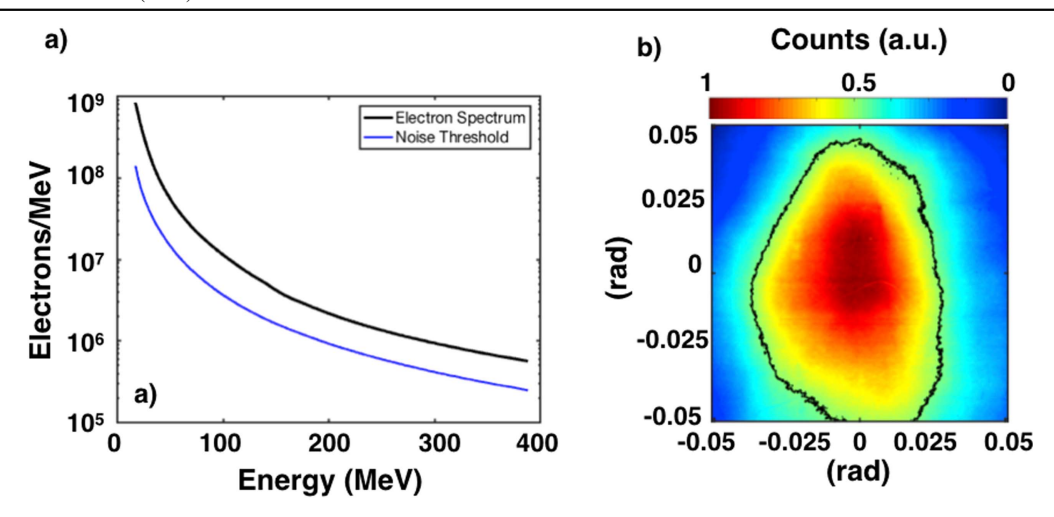


Figure 3. (a) Typical measured electron beam spectrum for a plasma density of  $5 \times 10^{18}$  cm<sup>-3</sup>. The blue curve represents the background noise on IP1, and the black curve the electron beam spectrum. (b) Typical electron beam shape recorded without the dispersion magnet where the black line represents the FWHM.

figure 3(a) for an electron density of  $5 \times 10^{18} \, \text{cm}^{-3}$  were the maximum observed electron energy is 380 MeV and the minimum measured energy is 18 MeV (limited by the diagnostic). The electron spectrum displays the typical exponentially decaying energy distribution with a two-temperature distribution of the form  $N_e \propto e^{-\frac{E}{T_1}} + e^{-\frac{E}{T_2}}$  where  $T_1$  is  $7 \pm 0.06$  MeV and  $T_2$  is  $30 \pm 0.9$  MeV. The electron beam shape was measured without the electron spectrometer (figure 3(b)). The electron beam is elliptical in the direction of the laser polarization with an average FWHM divergence of  $64 \times 100$  mrad. This ellipticity has been observed before and can be attributed to the residual transverse momentum [39] that the electrons gain at the moment of ionization and/or to DLA [27, 40]. The total charge of the electron beam was measured with an integrating current transformer placed 50 cm after the nozzle and without the electron spectrometer. The average total charge was 7.5 nC per shot for electron energies above 10 MeV. The electron spectrum for energies below 10 MeV can be extrapolated by fitting the measured spectrum thus the total beam charge including electron energies below 10 MeV increases to 10.5 nC. The total energy in the electron beam is estimated to be  $\sim$ 2 mJ, or  $\sim$ 0.002% of the laser energy.

#### 5. Bremsstrahlung source characterization

The objective of this work is to measure the bremsstrahlung radiation produced by the electrons propagating through the foil. In this experimental configuration, there are three simultaneous sources of x-ray radiation: betatron radiation from the SM-LWFA, bremsstrahlung radiation from electrons generated when the laser pulse (after exiting the gas jet) impinges on the foil and bremsstrahlung radiation from the electron beam passing through the foil. We therefore have to separately estimate the contribution of each source by adapting the experimental setup. The betatron radiation from the SM-LWFA was characterized by removing the foil and using the technique and

filters presented in [26]. When the foil is removed there is no bremsstrahlung radiation from the laser or electron beam, so betatron is the only x-ray source. The betatron signal recorded on IP2 was adjusted to a function of the form  $\frac{\mathrm{d}^2 I}{\mathrm{d}E\mathrm{d}\Omega} \propto A \left(\frac{E}{E_\mathrm{c}}\right)^2 K_{2/3}^2 \left[\frac{E}{E_\mathrm{c}}\right]$ , where E is the photon energy,  $E_\mathrm{c}$  is the critical energy,  $K_{2/3}$  is the modified Bessel function and A is the peak spectral density (photons  $keV^{-1}Sr^{-1}$ ). The measured critical energy for this experiment was  $18 \pm 10 \, \text{keV}$ , and A was  $5 \times 10^9$  photons keV<sup>-1</sup> Sr<sup>-1</sup>. To measure the radiation generated by the laser colliding with the foil, a shot with no gas puff was done with the foil 1.5 cm from the nozzle. No signal was recorded on IP2 since the laser intensity 1.5 cm from focus was reduced by four orders of magnitude. Thus, the signal recorded in the IP2 with the gas jet on and the foil in place is only affected by the betatron radiation and the bremsstrahlung radiation of the electron beam propagating through the foil. We assume the following intensity (I) distribution per unit photon energy dE and solid angle  $d\Omega$  as a function of the photon energy E for the generated radiation:

$$\frac{\mathrm{d}^2 I}{\mathrm{d}E\mathrm{d}\Omega} \propto B e^{-\frac{E}{E_{\mathrm{T}}}} + A \left(\frac{E}{E_{\mathrm{c}}}\right)^2 K_{2/3}^2 \left[\frac{E}{E_{\mathrm{c}}}\right]. \tag{1}$$

The first part of the expression represents the contribution from Bremsstrahlung radiation where  $E_{\rm T}$  is the temperature of the exponentially decaying Bremsstrahlung spectrum, and B is the peak spectral density. The second part is the contribution from the betatron radiation previously measured, where  $A=5\times10^9$  photons keV<sup>-1</sup> Sr<sup>-1</sup> and  $E_{\rm c}=18$  keV.

Figures 4(a)–(c) show the raw signals recorded on IP2 for the foils of Tungsten with thicknesses of 0.5 and 1 mm and Tantalum with a thickness of 1 mm, respectively. To analyze the data of figures 4(a)–(c), we subtracted the background of the IPs by performing a cubic interpolation around the signal recorded for each filter and subtracting that from the corresponding signal window on IP2. The results are shown in figures 4(d)–(f). The average Photostimulated luminescence

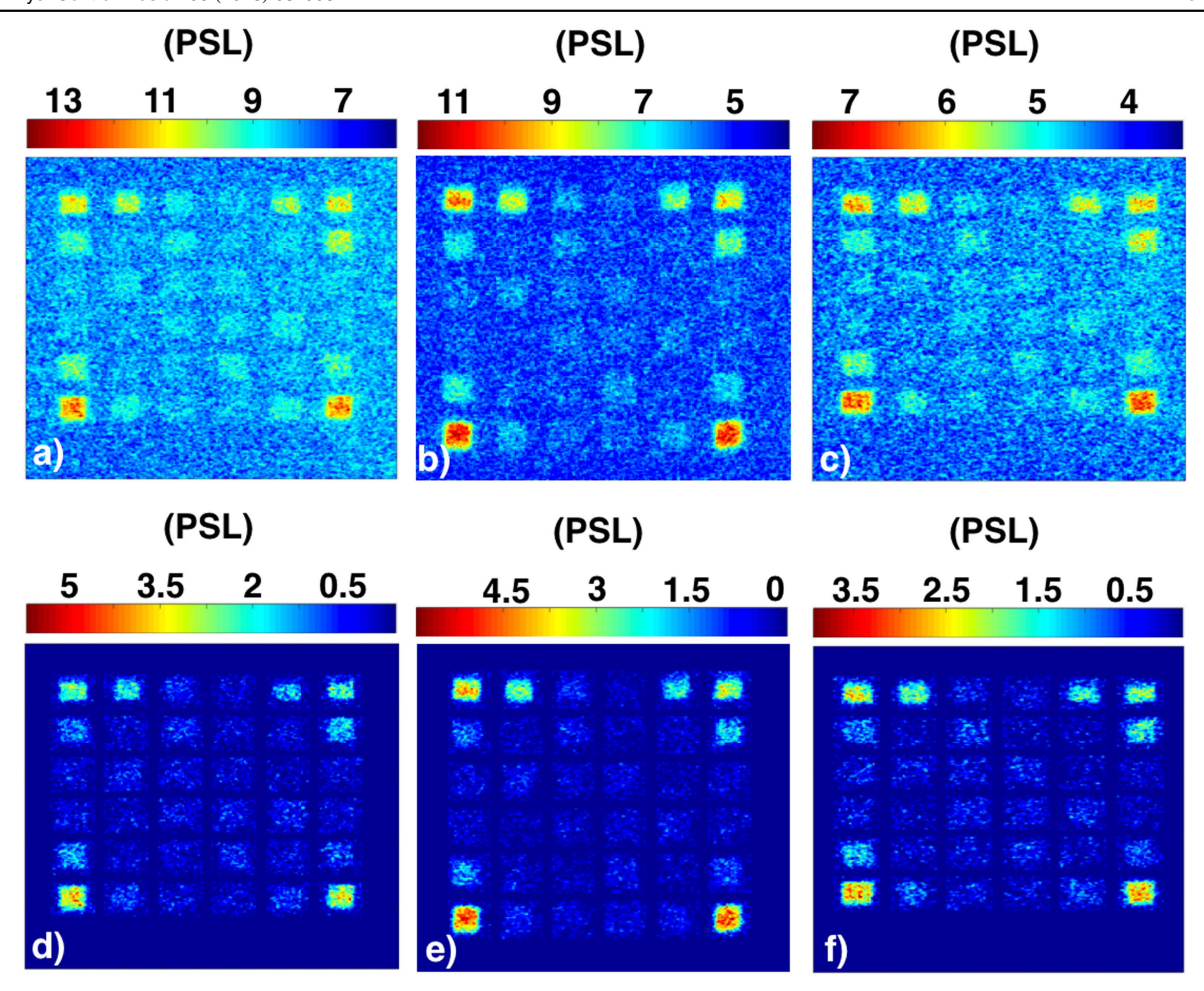


**Figure 4.** Signal recorded at the IP2 when using a Tungsten foil of (a) 1 mm, (b) 0.5 mm and a (c) 1 mm Tantalum foil. Background-corrected signal at the IP2 when using a Tungsten foil of (d) 1 mm, (e) 0.5 mm and a (f) 1 mm Tantalum foil. The images have the same orientation at figure 2(a).

signal in each of the channels is shown in figures 5(a), (c), (e) by the black dots for the 1 mm W, 1 mm Ta and 0.5 mm W foils, respectively. To obtain the spectrum of the produced radiation, we assumed an initial distribution function given by (equation (1)) and calculated the expected signal at IP2. A least squares fitting algorithm was used to fit the distribution function (equation (1)) to the experimental data (black dots in figures 5(a), (c) and (d)). The fit takes into account the propagation of the radiation through the aluminum and Mylar at the exit of the vacuum chamber, through each of the 36 filters of the step wedge filter and the sensitivity of IP2. For the betatron part of the distribution function, we also took into account the attenuation caused by the foil where the Bremsstrahlung radiation is generated. The best fit is shown by red line in figures 5(a), (c) and (e) and the shaded region shows the 95% confidence interval of the fit. Figures 5(b), (d) and (f), shows the hard x-ray energy spectrum for the best fitting parameters  $E_{\rm T}$  and  $B_{\rm t}$ , for the 1 mm W and Ta and 0.5 mm W foils, respectively. The 95% confidence interval is calculated from the fitting function for the fitting parameters  $E_T$  and B.

Since the calculated radiation has very high temperatures when compared to the betatron radiation and the step-wedge filter only detects radiation above 25 keV, we repeated the fitting procedure but now only considering the first part of equation (1) and the results were the same within the measurement accuracy level. From these results, we concluded that the yield of the betatron radiation is negligible when compared with the bremsstrahlung radiation from the electrons passing through the foil. The betatron yield at IP2 is so small because it is heavily filtered by the thick, high-Z foil placed after the nozzle. The foils do not transmit energies below 35 keV, and the measured  $E_{\rm c}$  of the betatron radiation was  $\sim$ 18 keV as explained above, thus most of the radiation does not make it through the foil.

The data shown in figure 5 can be used to compare the effect of material for a given thickness plus the effect of thickness for a given material. Figures 5(b) and (f) show that the spectrum temperature and amplitude is higher for the W foil  $(1978 \pm 534 \, \text{keV})$  when compared with Ta foil  $(1420 \pm 300 \, \text{keV})$ —i.e. Ta is lower but nevertheless within the error bar od the measurement. A small difference in amplitude and temperature is to be expected because the bremsstrahlung cross section directly depends on Z, and with such uncertainty in the measurement this difference cannot be measured experimentally. Figures 5(b) and (d) show that the

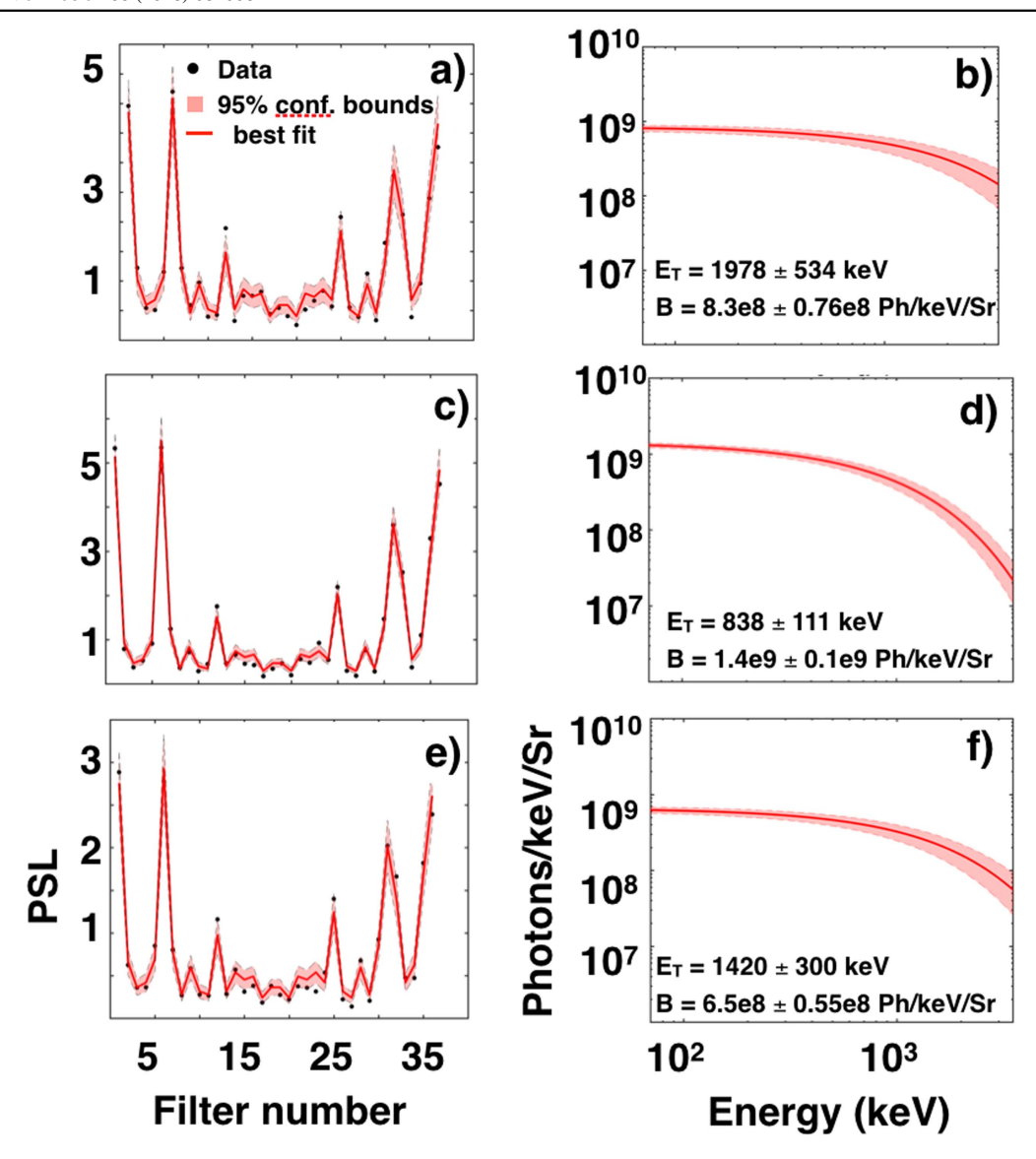


**Figure 5.** (a), (c) and (e) PSL counts at the IP after the hard x-ray crossed the filters of figure 2 (black dots) for the 1 mm and 0.5 mm W and 1 mm Ta foils, respectively. The red line is the best fit to the data points using equation (1), and the shaded region represents the 95% confidence intervals of the fits. (b), (d) and (f) hard x-ray energy spectrum for the best fitting parameters  $E_T$  and B, for the 1 mm and 0.5 mm W and 1 mm Ta foils, respectively.

0.5 mm foil (figure 5(f)) has a lower temperature spectrum than the 1 mm W foil. In the thinner foil, lower energy electrons have a higher contribution to the spectrum lowering the spectrum temperature. Also, the 0.5 mm foil has a higher yield for the lower energy photons because these can make it out of the target before being absorbed, unlike the 1 mm foil.

#### 6. Simulation results (GEANT 4)

The experimental data provided a measurement of the energy spectrum of the bremsstrahlung source, but to have a complete characterization, it is necessary to have source size and divergence. These quantities were not measured experimentally, but we used the code GEANT4 to get an estimate.

The GEANT4 development toolkit [41–43] is a Monte-Carlo code for particle transport calculations created for high-energy (MeV range) particle transport. It was used to simulate the electron beam transport and hard x-ray generation when an electron beam with the characteristics measured experimentally in section 4 propagates through a 1 mm W foil. The simulation used the Penelope [44] interaction library, which is designed for high-accuracy simulation of particle tracking in media without magnetic fields. This uses the most accurate high- and low-energy physics models in the investigated energy range [45, 46]. Below a given energy threshold, the energy loss (in this case 50 keV) is continuous and above it, the energy loss is simulated by explicit production of secondary particles. The target was represented as a rectangular box with  $100 \, \mathrm{mm} \times 100 \, \mathrm{mm}$  in the transverse (x and y) directions and a 1 mm thickness along the propagation (z) direction of electrons of solid W placed in the vacuum-filled volume. The electron energy spectrum presented in figure 3(a) was used as an input for the simulation,

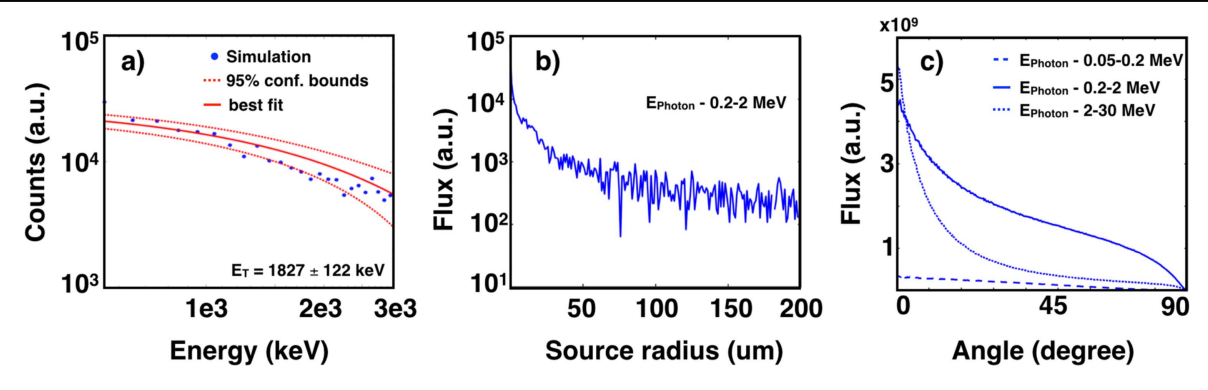


**Figure 6.** Results of a GEANT4 simulation of the generated bremsstrahlung radiation when an electron beam crosses a 1 mm W foil. (a) Simulated GEANT4 hard x-ray spectrum within a  $1^{\circ}$  angle, where the blue points show the simulations points, the solid red curve the best fit to the points using the bremsstrahlung contribution of equation (1), and the red dashed lines show the 95% confidence intervals of the fit. (b) Photon flux of the source in the 0.2-2 MeV range, within a  $1^{\circ}$  angle of the forward direction versus radius for a pencil-like electron beam impacting at the origin (x = y = z = 0) (c) Angular distribution for photon energies of 0.05-0.2 MeV (dashed), 0.2-2 MeV (solid) and 2-30 MeV (points).

and an extrapolation for electron energies lower then 18 MeV (minimum energy measured experimentally) was used. The electron source was considered point-like (at x = y = 0). Simulations were run for a total of 150 million events (electrons) and generated over 100 million high-energy (over 50 keV) photons, of which over 20 000 exited the target in the forward direction within a 1° cone half-angle. During the simulation, for each generated photon above an arbitrary threshold energy of 50 keV, the spatial coordinates and time for the generation, direction and kinetic energies at creation were recorded, and a virtual detector was set as a spherical shell with 120 mm radius around the target.

Figure 6(a) shows the simulated hard x-ray energy spectrum within a 1° angle (step wedge filter sees a 0.5° angle) in the forward propagation direction generated by an electron beam with the same characteristics as the one measured experimentally, as it propagates through a 1 mm W foil. The simulation points (blue) where fitted with the bremsstrahlung contribution of equation (1) to determine the temperature of the spectrum, which was  $1827 \pm 122 \, \text{keV}$ . This temperature is in close agreement with the experimental value of  $1978 \pm 534 \, \text{keV}$ .

Figure 6(b) shows the photon flux of the source in the 0.2–2 MeV range, within a 1° angle of the forward direction versus transverse radius for a pencil-like electron beam impacting at the origin (x = y = z = 0). The distance (radius) also corresponds to how far the electrons traveled transversally (x and y directions) from the point of impact. This source profile has a very sharp peak (FWHM estimated to be 1.1  $\mu$ m) on a relatively shallow pedestal, with 50% of the total photons emitted within  $8 \mu m$  radius. This flux profile can be convolved with an electron beam profile (assuming homogeneous electron energy distribution) to estimate the profile of the electron beam. Taking the beam profile shown in figure 3(b), the electron beam at 15.5 mm (midpoint of the W plate) would have the size of 987  $\mu$ m  $\times$  1557  $\mu$ m, while the x-ray source size gained from convolution was  $987 \times 1559 \,\mu\text{m}$ , effectively identical to the size of the electron beam at the target position. It should be noted that the source size can be reduced by placing the foil closer to the exit of the gas jet as seen by [16].

The divergence of the source for the three energy bins is shown in figure 6(c). The half angle (at half maximum) for the energy bin of 0.05–0.2 MeV is 35°, for 0.2–2 MeV is 28°, for 2–30 MeV is 9°, and 12.4° considering the whole 0.05–30 MeV photon energy range. The divergence of the source decreases with photon energy, scaling with the photon energy approximately as  $E_{\rm photon}^{-0.5}$ . These above divergence numbers are for a non-diverging electron beam. For reference, the half-angle-at-half-maximum divergence of the e-beam profile shown in figure 3(b) is 2.9°.

#### 7. Conclusions

We have produced and characterized a bremsstrahlung source based on a SM-LWFA suitable for use in HEDS facilities with kJ-class lasers. The radiation is emitted when the electron beam, produced by SM-LWFA, collides with a high-Z foil placed downstream. The electron beams can be fitted with a two-temperature spectrum and exhibit a high beam charge of 7.5 nC for electron energies above 10 MeV. Using a tungsten or tantalum converter, we have demonstrated the production of hard x-rays with temperatures from 0.8 to 2 MeV and up to 10<sup>9</sup> Photons keV<sup>-1</sup> Sr<sup>-1</sup>, which represents an improvement of at least two orders of magnitude in the number of photons when compared to the LWFA blowout regime [16]. According to the Monte-Carlo simulation using GEANT4, the x-ray source size in the setup is minimally influenced by the electron transport within the target foil, rather it is determined by the divergence and size of the electron beam impinging on the foil. As the travel distance of the electrons within the foil is almost negligible compared to the electron beam diameter, an x-ray source size of  $0.95 \, \mathrm{mm} \times 1.5 \, \mathrm{mm}$  was inferred (that matches the size of the electron beam on the foil) as well as a divergence of half angle (at half-maximum) of 12.4°.

This hard x-ray source could be used as a probe for opacity/radiography measurements at NIF that can require

photon energies up to a few MeV to study high-Z materials in HED conditions or for imaging double-shell ignition targets. The photon distribution temperature and flux can be controlled by changing the electron energy of the SM-LWFA, and the source size can be controlled by changing the distance from the electron source to the converter foil or by reducing the size of the converter foil (using high-Z thin wires).

#### **Acknowledgments**

This work was partially supported POCI/FIS/59574/2004, by the auspices of the US Department of Energy by Lawrence Livermore National Laboratory under the contract DE-AC52-07NA27344. Lawrence Livermore National Security, LLC, and DOE Early Career Research Prog. SCW1575/1. LLNL-JRNL-742178, and the work the of UCLA colleagues was supported by DOE fund De-SC0010064, NNSA grant DE-NA0002950 and NSF grant 1734315. J. L. Shaw was supported by the Department of Energy and the National Science Foundation under grant DESC0017950.

#### **ORCID iDs**

N Lemos https://orcid.org/0000-0002-6781-5672 J L Shaw https://orcid.org/0000-0002-1118-8921

#### References

- [1] Goldsack T J et al 2002 IEEE Trans. Plasma Sci. 30 239
- [2] Amendt P et al 2007 Phys. Plasmas 14 056312
- [3] Tommasini R et al 2011 Phys. Plasmas 18 056309
- [4] Glinec Y et al 2005 Phys. Rev. Lett. 94 025003
- [5] Courtois C et al 2013 Phys. Plasmas 20 083114
- [6] Courtois C et al 2011 Phys. Plasmas 18 023101
- [7] Perry M D et al 1999 Rev. Sci. Instrum. 70 265
- [8] Courtois C et al 2009 Phys. Plasmas 16 013105

- [9] Norreys P A et al 1999 Phys. Plasmas 6 2150
- [10] Hatchett S P et al 2000 Phys. Plasmas 7 2076
- [11] Anthony L et al 2012 IEEE Trans. Plasma Sci. 40 8
- [12] Tajima T and Dawson J M 1979 Phys. Rev. Lett. 43 267-70
- [13] Edwards R D et al 2002 Appl. Phys. Lett. 80 2129
- [14] Galy J et al 2007 New J. Phys. 9 23
- [15] Ben-Ismail A et al 2011 Appl. Phys. Lett. 98 264101
- [16] Döpp A et al 2016 Nucl. Instrum. Methods Phys. Res. A 830 515-9
- [17] Lu W 2007 Phys. Rev. ST Accel. Beams 10 061301
- [18] Pukhov A et al 1999 Phys. Plasmas 6 2847
- [19] Geddes C G R et al 2004 Nature 431 538-41
- [20] Mangles S P D et al 2004 Nature 431 535-8
- [21] Faure J et al 2004 Nature 431 541-4
- [22] Esarey E, Krall J and Sprangle P 1994 Phys. Rev. Lett. 72 2887
- [23] Sprangle P et al 1992 Phys. Rev. Lett. 69 2200
- [24] Modena A 1995 Nature 377 606-8
- [25] Forslund D W, Kindel J M, Mori W B, Joshi C and Dawson J M 1985 Phys. Rev. Lett. 54 6
- [26] Albert F et al 2017 Phys. Rev. Lett. 118 134801
- [27] Shaw J L et al 2017 Phys. Rev. Lett. 118 064801
- [28] Pukhov A, Sheng Z-M and Meyer-ter Vehn J 1999 Phys. Plasmas 6 2847
- [29] Shaw J L et al 2014 Plasma Phys. Control. Fusion 56 084006
- [30] Zhang X, Khudik V N and Shvets G 2015 Phys. Rev. Lett. 114 184801
- [31] Lemos N et al 2016 Plasma Phys. Control. Fusion 58 034018
- [32] Lemos N et al 2009 Rev. Sci. Instrum. 80 103301
- [33] Thomas A G R et al 2007 Phys. Rev. Lett 98 054802
- [34] Williams G J et al Rev. Sci. Inst. in preparation
- [35] Tommasini R et al 2017 Phys. Plasmas 24 053104
- [36] Hui Chen et al 2012 Rev. Sci. Inst. 83 10E113
- [37] Tommassini R et al 2008 Rev. Sci. Inst. 79 10E901
- [38] Maddox B R et al 2011 Rev. Sci. Instrum. 83 023111
- [39] Thaury C 2013 Phys. Rev. Lett. 111 135002
- [40] Mangles S P D et al 2006 Phys. Rev. Lett. 96 215001
- [41] Agostinelli S et al 2003 Nucl. Instrum. Methods Phys. Res. A 506 250–303
- [42] Allison J et al 2006 IEEE Trans. Nucl. Sci. 53 270-8
- [43] Allison J et al 2016 Nucl. Instrum. Methods Phys. Res. A 835 186–225
- [44] Baró J, Sempau J, Fernández-Varea J and Salvat F 1995 Nucl. Instr. Methods Phys. Res. B 100 31–46
- [45] Pandola L, Andenna C and Caccia B 2015 NIM B 41 350
- [46] Faggedon B A et al 2008 Med. Phys. 35 4308